ELSEVIER

A waveguide finite element and boundary element approach to calculating the sound radiated by railway and tram rails

C.-M. Nilsson, C.J.C. Jones[*], D.J. Thompson, J. Ryue

Institute of Sound and Vibration Research, University of Southampton, Southampton SO17 1BJ, UK

Abstract

Engineering methods for modelling the generation of railway rolling noise are well established. However, these necessarily involve some simplifying assumptions to calculate the sound powers radiated by the wheel and the track. For the rail, this involves using an average vibration together with a radiation efficiency determined for a two-dimensional (2D) problem. In this paper, the sound radiation from a rail is calculated using a method based on a combination of waveguide finite elements and wavenumber boundary elements. This new method allows a number of the simplifying assumptions in the established methods to be avoided. It takes advantage of the 2D geometry of a rail to provide an efficient numerical approach but nevertheless takes into account the three-dimensional nature of the vibration and sound field and the infinite extent of the rail. The approach is used to study a conventional 'open' rail as well as an embedded tram rail of the type used for street running. In the former case it is shown that the conventional approach gives correct results and the complexity of the new method is mostly not necessary. However, for the embedded rail it is found that it is important to take into account the radiation from several wave types in the rail and embedding material. The damping effect of the embedding material on the rail vibration is directly taken into account and, for the example shown, causes the embedded rail to radiate less sound than the open rail above about 600 Hz. The free surface of the embedding material amplifies the sound radiation at some frequencies, while at other frequencies it moves out of phase with the rail and reduces the radiation efficiency. At low frequencies the radiation from the embedded rail resembles a line monopole source which produces greater power than the 'open' rail which forms a line dipole.

1. Introduction

The most important source of environmental noise from railways is rolling noise, in which the track and wheels are excited into vibration by the 'roughness' of the running surfaces. Both the wheels and the track radiate significant components of noise [1,2], their relative importance depending on details of the design, the roughness spectra and the train speeds. Nevertheless, the component of noise from the rail is often the highest, particularly for the lower running speeds typical of light rail systems.

*Corresponding author. Tel.: +44 23 8059 3224; fax: +44 23 8059 3190.

E-mail address: cjcj@isvr.soton.ac.uk (C.J.C. Jones).

Many light rail or tram systems rely on street running, for which the rails are embedded in the road surface. This introduces important differences in the response and sound radiation of a rail which need to be investigated. Moreover, slab tracks are also being considered for heavy rail applications in order to provide higher infrastructure availability over conventional ballasted track. A number of ballastless, or 'slab', track designs have been put forward in recent years. In particular, some of these low-maintenance track concepts include continuous support of the rail either on top of the supporting concrete slab or embedded in the slab, e.g. Refs. [3,4].

Engineering methods for predicting rolling noise were first developed by Remington [5,6], and later extended by Thompson [7]. A software package was produced, shared by a number of railway research organisations and known as TWINS ('Track-Wheel Interaction Noise Software') [8,9]. Within TWINS, the track vibration can be calculated by one of several methods, either based on a Timoshenko beam or using a periodic structure model based on finite elements (FEs) [10,11]. These are used to predict the spatially averaged vibration in each of a number of waves due to the wheel/rail contact forces. The sound radiation from these waves is determined using radiation efficiencies obtained for a 2D geometry. Although this approach clearly involves a number of simplifying assumptions, it has been shown that the use of 2D radiation efficiencies is usually justified [12]. The model has been used to good effect to design a wide variety of low-noise wheels and tracks [13].

The purpose of this paper is to introduce a new approach for determining the vibration and sound radiation from a rail, which allows several of the simplifying assumptions in the established methods to be avoided. This will be of particular use for slab tracks and embedded rails. It uses a combination of waveguide FEs and wavenumber boundary elements (BEs). This takes advantage of the 2D geometry of a rail to provide an efficient numerical approach; nevertheless it takes into account the three-dimensional (3D) nature of the vibration and sound field and the infinite extent of the rail.

Waveguide (or spectral) FEs are used to represent structures which have a 2D geometry (here denoted the y–z plane), while having a constant cross-section in the third (x) direction. A FE mesh is formed in the y–z plane, with the usual assumptions of shape functions, while a wave-type solution is assumed in the x direction. Such an approach has been used to study a variety of problems including rods [14], composite plates [15], thin-walled beams [16], rib-stiffened plates [17], pipes [18] and car tyres [19]. This method can be used to determine the free waves propagating (dispersion relation) or to find the forced response as a function of frequency. In the latter case, it is necessary to solve a series of 2D problems for different wavenumbers in the x direction. The overall response is then recovered using an inverse Fourier transform.

A similar method has also been used previously to study the waves propagating in railway rails by Knothe et al. [20], Gavric [21] and Bartoli et al. [22]. In each case these considered only the free waves propagating in an unsupported rail. Ryue et al. [23] have used this approach to determine the waves propagating in a supported rail up to 80 kHz. Models of the forced response of a railway track based on this approach, but including the effects of periodic supports, have been developed by Gry [24,25] and Gomez et al. [26].

In the present paper, the waveguide FE approach is used to calculate the vibration of an infinite, continuously supported rail excited by a point force. From this response, the acoustic radiation is calculated using the wavenumber BE approach [27,28]. In the same way as for the vibration, this involves the solution of a series of 2D radiation problems for different wavenumbers in the x direction, the overall solution being recovered via an inverse Fourier transform. The novelty of the current paper lies in the combined use of these two techniques and their application to the problem of noise radiation by a rail. As both methods operate in the wavenumber domain, it is straight-forward to couple them together, although it should be pointed out that there is no need, in the present case, to solve a fully coupled problem, the surface vibration being used simply as an input to the acoustic radiation problem.

In Sections 2 and 3 the theory of waveguide FE and wavenumber BE methods is reviewed. The combined waveguide FE and wavenumber BE approach is applied to the study of a conventional 'open' rail in Section 4 and an embedded tram rail in Section 5. In the former case, it is used to validate the existing simplified approach, but for the embedded rail some additional features of the response and radiation are explored.

2. Waveguide FE model

This section describes the theory of the waveguide FE method and the next section summarises the acoustic BE method transformed to the wavenumber domain along the rails. These methods are applied to a prismatic geometry, as shown in Fig. 1, where the cross-section A in the y–z plane is constant with x. Harmonic motion at frequency ω is assumed with an implicit time dependence $e^{i\omega t}$.

A derivation of a waveguide FE model can be made in various ways. The derivation described here is based on Hamilton's principle, which in the frequency domain for a solid can be written as

$$\delta U(\omega) - \delta T(\omega) - \delta W(\omega) = 0 \tag{1}$$

where δ denotes 'the first variation of', U and T are the potential and kinetic energies in the system and δW is the virtual work on the structure. Each of the terms of the left-hand side of Eq. (1) is examined separately in Sections 2.1–2.3.

2.1. Potential energy

The first variation of the potential energy in a volume V may be written as

$$\delta U(\omega) = \int_V \delta\boldsymbol{\varepsilon}^{\mathrm{H}} \mathbf{D}\boldsymbol{\varepsilon} \, \mathrm{d}V \tag{2}$$

where $\boldsymbol{\varepsilon} = [\varepsilon_x \; \varepsilon_y \; \varepsilon_z \; \gamma_{xy} \; \gamma_{xz} \; \gamma_{yz}]^{\mathrm{T}}$ are the strain amplitudes in the material, $^{\mathrm{H}}$ denotes the complex conjugate transpose and $\mathbf{D}$ is a material stiffness matrix given in Appendix A. The strains can be written in terms of the displacements as

$$\boldsymbol{\varepsilon} = \left(\mathbf{B}_0 + \mathbf{B}_1 \frac{\partial}{\partial x} \right) \mathbf{u} \tag{3}$$

where $\mathbf{u} = [u \; v \; w]^{\mathrm{T}}$ contains the displacement amplitudes in the x, y and z directions. $\mathbf{B}_0$ and $\mathbf{B}_1$ are linear matrix operators comprising first and zero order spatial derivatives with respect to the y and z coordinates. These operators are also given in Appendix A.

The displacements in $\mathbf{u}$ and the virtual displacements in $\delta\mathbf{u}$ can be approximated by

$$\mathbf{u} = \mathbf{N}(y,z)\hat{\mathbf{u}}(x) \quad \text{and} \quad \delta\mathbf{u} = \mathbf{N}(y,z)\delta\hat{\mathbf{u}}(x) \tag{4}$$

where $\mathbf{N}(y,z)$ are conventional 2D FE shape functions and $\hat{\mathbf{u}}$ and $\delta\hat{\mathbf{u}}$ are nodal values for the displacements and virtual displacements. In this paper eight-noded isoparametric quadrilateral elements are used, so that the shape functions $\mathbf{N}(y,z)$ are chosen to be quadratic polynomial functions.

Inserting Eqs. (3) and (4) into Eq. (2) yields

$$\delta U(\omega) = \int_x \sum_{i=0}^{1} \sum_{j=0}^{1} \frac{\partial^i \delta\hat{\mathbf{u}}^{\mathrm{H}}}{\partial x^i} \mathbf{a}_{ij} \frac{\partial^j \hat{\mathbf{u}}}{\partial x^j} \, \mathrm{d}x \tag{5}$$
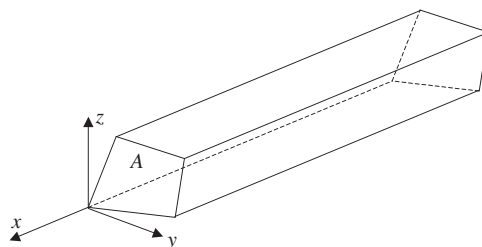

Fig. 1. Geometry of a typical waveguide finite element.

where the element stiffness and higher order stiffness matrices, $\mathbf{a}_{ij}$, are defined by

$$\mathbf{a}_{ij} = \int_A [\mathbf{B}_i \mathbf{N}]^\mathrm{T} \mathbf{D} [\mathbf{B}_j \mathbf{N}] \, \mathrm{d}A \tag{6}$$

These 2D integrations over the cross-section are made numerically by Gauss quadrature, as detailed in textbooks on FE methods, e.g., Ref. [29].

2.2. Kinetic energy

The first variation of the kinetic energy in a volume V in the frequency domain is given by

$$\delta T(\omega) = \rho_m \omega^2 \int_V \delta \mathbf{u}^\mathrm{H} \mathbf{u} \, \mathrm{d}V \tag{7}$$

where ρ_m is the material density. Using the same shape function approximation as before gives

$$\delta T(\omega) = \omega^2 \int_x \delta \hat{\mathbf{u}}^\mathrm{H} \mathbf{m} \hat{\mathbf{u}} \, \mathrm{d}x \tag{8}$$

where the element mass matrix $\mathbf{m}$ is given by

$$\mathbf{m} = \int_A \rho_m \mathbf{N}^\mathrm{T} \mathbf{N} \, \mathrm{d}A \tag{9}$$

which is evaluated using Gauss quadrature in the same way as for the other element matrices.

2.3. Virtual work

The virtual work is considered to arise from external forces and internal losses. For simplicity the virtual work from the losses, i.e. the damping, is approximated by amending $\mathbf{D}$ by adding an imaginary part such that,

$$\mathbf{D} = Re\{\mathbf{D}\}(1 + i\eta) \tag{10}$$

where η is the damping loss factor.

The virtual work due to external forces, δW_e may be written as

$$\delta W_e(\omega) = \int_V \delta \mathbf{u}^\mathrm{H} \mathbf{f} \, \mathrm{d}V \tag{11}$$

where $\mathbf{f}$ is a vector comprising the external forces in the x, y and z directions. Thus with the FE shape function approximation from Eq. (4), a weighted force vector, $\hat{\mathbf{f}}$, can be defined through

$$\delta W_e = \int_x \delta \hat{\mathbf{u}}^\mathrm{H} \left(\int_A \mathbf{N}^\mathrm{T} \mathbf{f} \, \mathrm{d}A \right) \mathrm{d}x = \int_x \delta \hat{\mathbf{u}}^\mathrm{H} \hat{\mathbf{f}} \, \mathrm{d}x \tag{12}$$

where $\hat{\mathbf{f}}$ is the term within brackets. Usually appropriate forces may be directly applied on the nodes of the FE model.

2.4. Complete FE model

Inserting these expressions for δU, δT and δW, i.e. Eqs. (5), (8) and (12), into Eq. (1), yields,

$$\int_x \left(\sum_{i=0}^1 \sum_{j=0}^1 \frac{\partial^i \delta \hat{\mathbf{u}}}{\partial x^i} \mathbf{a}_{ij} \frac{\partial^j \hat{\mathbf{u}}}{\partial x^j} - \omega^2 \delta \hat{\mathbf{u}}^\mathrm{H} \mathbf{m} \hat{\mathbf{u}} - \delta \hat{\mathbf{u}}^\mathrm{H} \hat{\mathbf{f}} \right) \mathrm{d}x = 0 \tag{13}$$

The matrices $\mathbf{a}_{ij}$ and $\mathbf{m}$ must be evaluated for each element.

Assembling all elements in the model so that shared nodes have the same displacements and internal forces are eliminated means that Eq. (13) can be rewritten in a similar form, but including all degrees of freedom of the FE model. The degrees of freedom for all FE displacements are now the entries in the system vector $\hat{\mathbf{U}}$.

Integration by parts with respect to the x-coordinate follows. Dropping the integral and the virtual displacements, $\delta\hat{\mathbf{U}}$ is justified by the calculus of variations, see e.g. Ref. [30]. The equation of motion is subsequently written as

$$\left[\mathbf{K}_2\frac{\partial^2}{\partial x^2} + \mathbf{K}_1\frac{\partial}{\partial x} + \mathbf{K}_0 - \omega^2\mathbf{M}\right]\hat{\mathbf{U}} - \hat{\mathbf{F}} = \mathbf{0} \tag{14}$$

Performing a Fourier transform of this system from the x-coordinate to the wavenumber domain gives

$$[\mathbf{K}_2(-\mathrm{i}\kappa)^2 + \mathbf{K}_1(-\mathrm{i}\kappa) + \mathbf{K}_0 - \omega^2\mathbf{M}]\tilde{\mathbf{U}} = \tilde{\mathbf{F}} \tag{15}$$

where κ is the wavenumber in the x-direction and $\sim$ indicates the Fourier transformed properties in this wavenumber domain, given by the Fourier transform pair

$$\tilde{\mathbf{U}}(\kappa) = \int_{-\infty}^{\infty}\tilde{\mathbf{U}}(x)\mathrm{e}^{\mathrm{i}\kappa x}\,\mathrm{d}x \tag{16}$$

$$\tilde{\mathbf{U}}(x) = \frac{1}{2\pi}\int_{-\infty}^{\infty}\tilde{\mathbf{U}}(\kappa)\mathrm{e}^{-\mathrm{i}\kappa x}\,\mathrm{d}\kappa \tag{17}$$

and similarly for $\tilde{\mathbf{F}}$.

2.5. Eigenvalue solutions

In the absence of external forces, $\tilde{\mathbf{F}} = \mathbf{0}$, Eq. (15) represents a double eigenvalue problem:

$$[\mathbf{K}_2(-\mathrm{i}\kappa)^2 + \mathbf{K}_1(-\mathrm{i}\kappa) + \mathbf{K}_0 - \omega^2\mathbf{M}]\tilde{\mathbf{U}}_R = \mathbf{0} \tag{18}$$

This is a linear eigenvalue problem in frequency ω for a given wavenumber κ, or equivalently a quadratic eigenvalue problem in wavenumber κ for a given frequency ω. The latter form yields a set of complex-valued wavenumbers κ_n and the corresponding eigenvectors for each frequency. The right and left eigenvectors are denoted $\tilde{\mathbf{U}}_{nR}$ and $\tilde{\mathbf{U}}_{nL}$, respectively. Numerical solution methods for quadratic eigenvalue problems are discussed comprehensively in Ref. [31].

2.6. Solution for a point force

A point force at $x = 0$ can be represented by a constant force vector $\tilde{\mathbf{F}}_0$ at all wavenumbers describing the force distribution over the cross-section. The resulting response in Eq. (15), denoted $\tilde{\mathbf{U}}_0$, can be found for a range of wavenumbers κ at each frequency using standard matrix solvers. The solution in the spatial domain can then be recovered by a discrete inverse Fourier transform, see Eq. (17). However, since the solution is dominated by slowly decaying waves, appearing as very narrow peaks in the wavenumber domain, the range of wavenumbers must be quite narrowly spaced for the result to converge. An alternative method is therefore used.

For $x \geqslant 0$ the integral in Eq. (17) can be replaced by a contour integral around the lower half plane, where κ may now be complex. If $x < 0$ the integral is instead made over the upper half plane. Limiting discussion to the case $x \geqslant 0$, the solution to the integral is given by the sum of the residues of the poles in the lower half plane, $Im(\kappa) < 0$. These poles are the eigenvalues, κ_n, discussed in the previous section. The solution for $\hat{\mathbf{U}}_0$ written as a sum of residues, see Refs. [32,33], becomes

$$\hat{\mathbf{U}}_0(x) = \mathrm{i}\sum_n\frac{\tilde{\mathbf{U}}_{nL}\tilde{\mathbf{F}}_0}{\tilde{\mathbf{U}}_{nL}\mathbf{D}'(\kappa_n)\tilde{\mathbf{U}}_{nR}}\tilde{\mathbf{U}}_{nR}\mathrm{e}^{-\mathrm{i}\kappa_n x} \quad \text{for } x \geqslant 0 \tag{19}$$

where

$$
\begin{aligned}
\mathbf{D}'(\kappa_n) &= \frac{\partial}{\partial \kappa}[\mathbf{K}_2(-i\kappa)^2 + \mathbf{K}_1(-i\kappa) + \mathbf{K}_0 - \omega^2\mathbf{M}]_{\kappa=\kappa_n} \\
&= -2\kappa_n\mathbf{K}_2 - i\mathbf{K}_1
\end{aligned}
\tag{20}
$$

The solution for $x < 0$ is symmetric with that for $x \geqslant 0$.

2.7. Convolution with force distribution

The constant force vector $\tilde{\mathbf{F}}_0$, corresponding to a point force at $x = 0$, gives unrealistic solutions at that location when the size of the FE model and the number of waves increase. To overcome this, a half-cosine force distribution along the x-direction is assumed

$$
\hat{f}(x) = \begin{cases} \dfrac{\beta}{2}\cos(\beta x) & \text{for} \quad -\dfrac{\pi}{2\beta} \leqslant x \leqslant \dfrac{\pi}{2\beta} \\ 0 & \text{otherwise} \end{cases}
\tag{21}
$$

where π/β is the length of the excitation region and the distribution has a unit resultant. The Fourier transform of $\hat{f}(x)$ is

$$
\tilde{f}(\kappa) = \frac{\cos\left(\dfrac{\pi\kappa}{2\beta}\right)}{1 - \left(\dfrac{\kappa}{\beta}\right)^2}
\tag{22}
$$

The overall force acting in Eq. (15) is now $\tilde{\mathbf{F}}_0\tilde{f}$, so that the response in the wavenumber domain can be calculated using the product of Eq. (22) with $\tilde{\mathbf{U}}_0$. The response to this force distribution can also be found from the convolution of the solution in the spatial domain, $\hat{\mathbf{U}}_0$, with the force distribution $\hat{f}(x)$,

$$
\hat{\mathbf{U}}(x) = \int_{-\infty}^{\infty} \hat{\mathbf{U}}_0(x - \xi)\hat{f}(\xi)\,d\xi
\tag{23}
$$

Evaluating this for $x = 0$, and noting that $\hat{f}(x) = 0$ outside the forcing region and that both $\hat{f}$ and $\hat{\mathbf{U}}_0$ are symmetric,

$$
\begin{aligned}
\hat{\mathbf{U}}(0) &= \int_{-\pi/2\beta}^{\pi/2\beta} \sum_n A_n \tilde{\mathbf{U}}_{nR}\, e^{-i\kappa_n|\xi|} \frac{\beta}{2}\cos(\beta\xi)\,d\xi \\
&= \sum_n A_n \tilde{\mathbf{U}}_{nR} \frac{-i\lambda - e^{-i\pi\lambda/2}}{\lambda^2 - 1}
\end{aligned}
\tag{24}
$$

where $\lambda = \kappa_n/\beta$ and

$$
A_n = \frac{i\tilde{\mathbf{U}}_{nL}\tilde{\mathbf{F}}_0}{\tilde{\mathbf{U}}_{nL}\mathbf{D}'(\kappa_n)\tilde{\mathbf{U}}_{nR}}
\tag{25}
$$

Eq. (24) is used to predict the frequency response function of the track. However, as will be seen, to predict the acoustic radiation it is useful to obtain the solution in the wavenumber domain. This can be obtained by taking the Fourier transform of $\hat{\mathbf{U}}_0$ from Eq. (19). This Fourier transform can be evaluated as

$$
\begin{aligned}
\tilde{\mathbf{U}}_0(\kappa) = \sum_n A_n \tilde{\mathbf{U}}_{nR} &\left(\frac{-1}{Im(\kappa_n) - i(\kappa + Re(\kappa_n))} \right. \\
&\left. + \frac{-1}{Im(\kappa_n) + i(\kappa - Re(\kappa_n))} \right)
\end{aligned}
\tag{26}
$$

Then $\tilde{\mathbf{U}}(\kappa)$ can be found by multiplying this by $\tilde{f}(\kappa)$ from Eq. (22). Since both $\tilde{f}(\kappa)$ and $\tilde{\mathbf{U}}_0(\kappa)$ are given as closed form expressions, the range of wavenumbers can be chosen such that they are more finely spaced in the vicinity of the poles.

3. Inclusion of the acoustic domain

3.1. Wave domain BE model

The acoustic properties of the fluid system may be described by the Helmholtz equation and a boundary integral. The Helmholtz equation here takes the form, see e.g. Ref. [34],

$$\Delta\hat{\Psi} + k^2\hat{\Psi} = q(\mathbf{r}) \tag{27}$$

where Δ is the 3D Laplace operator, $\hat{\Psi}$ is the velocity potential for the fluid, $q(\mathbf{r})$ describes the sources in the fluid, $k = \omega/c$ is the wavenumber for freely propagating waves in the fluid and c is the velocity of sound. The fluid particle velocity, $\hat{v}_n$, in direction $\mathbf{n}$ and the fluid acoustic pressure $\hat{p}$ are given by

$$\hat{v}_n = \mu\frac{\partial\hat{\Psi}}{\partial\mathbf{n}} \tag{28}$$

and

$$\hat{p} = \mathrm{i}\omega\mu\rho_0\hat{\Psi} \tag{29}$$

where $\mathbf{n}$ is a unit direction vector, μ is a scalar constant introduced to improve the conditioning in the resulting numerical problem and ρ_0 is the fluid density.

In addition to Eq. (27) a boundary equation is needed to encompass natural boundary conditions. Here the following form is used, see e.g. Ref. [35],

$$\int_S\left(\delta\hat{\Psi}^*\frac{\partial\hat{\Psi}}{\partial\mathbf{n}} - \hat{\Psi}\frac{\partial(\delta\hat{\Psi}^*)}{\partial\mathbf{n}}\right)\mathrm{d}S = 0 \tag{30}$$

where S is the surface of the boundary domain and * indicates complex conjugate. From Eq. (27), performing a Fourier transform from the coordinate along the x-axis to the wavenumber domain (assuming constant geometry) for the case of no sources within the fluid gives

$$\Delta_{2D}\tilde{\Psi} + (k^2 - \kappa^2)\tilde{\Psi} = 0 \tag{31}$$

where $\Delta_{2D} = \partial^2/\partial y^2 + \partial^2/\partial z^2$ and κ is the wavenumber in the x-direction.

The Fourier transform leaves Eq. (30) unchanged except that the surface integral now becomes a line integral over the perimeter Γ,

$$\int_\Gamma\left(\delta\tilde{\Psi}^*\frac{\partial\tilde{\Psi}}{\partial\mathbf{n}} - \tilde{\Psi}\frac{\partial(\delta\tilde{\Psi}^*)}{\partial\mathbf{n}}\right)\mathrm{d}\Gamma = 0 \tag{32}$$

Eq. (31) differs from a normal 2D Helmholtz equation in that k^2 is replaced by $(k^2 - \kappa^2)$. When $k^2 > \kappa^2$ and the fluid is undamped, this system can be described with a normal 2D BE model by replacing k with the variable α defined by

$$\alpha = \sqrt{k^2 - \kappa^2} \tag{33}$$

On the other hand, if $k^2 < \kappa^2$, Eq. (31) will result in an acoustic nearfield solution rather than a wave solution. Since nearfield solutions radiate no sound power, it is not necessary to include these solutions here. Hence the sound power radiation can be described by a normal 2D BE model by replacing k with α. The software used here is a modified version of the 2D BE model described in Ref. [35]. The result from the BE model gives a relation between $\hat{\Psi}$ and $\partial\hat{\Psi}/\partial\mathbf{n}$, where $\mathbf{n}$ is the normal unit vector to the surface of the rail structure.

This relation may be written as

$$\mu \mathbf{H} \tilde{\boldsymbol{\Psi}} - \mu \mathbf{G} \frac{\partial \tilde{\boldsymbol{\Psi}}}{\partial \mathbf{n}} = \mathbf{0} \qquad (34)$$

where $\tilde{\boldsymbol{\Psi}}$ and $\partial \tilde{\boldsymbol{\Psi}}/\partial \mathbf{n}$ are vectors of the respective variable at the nodes of the BE model. If so called 'CHIEF' points are used to overcome the non-uniqueness problem associated with internal resonances, $\mathbf{H}$ and $\mathbf{G}$ have more rows than columns [36].

In addition to Eq. (34) more equations are needed to determine the system fully. These describe essential boundary conditions so that local values of the pressures, normal velocities or local impedances at the boundary are given. In addition they relate the normal velocities to displacements of the FE model.

3.2. Coupling between FE and BE models

The finite and BE models are constructed in such a way that the nodes of the respective models share the same coordinates at the surface where they are connected and have compatible shape functions. Furthermore, the air will have negligible influence on the vibrations of the rail so that a fully coupled model is not necessary. The coupling condition at the shared node coordinates i is then simply,

$$\hat{v}_{ni} = \mathrm{i}\omega \hat{\mathbf{u}}_i \cdot \mathbf{n} \qquad (35)$$

where '$\cdot$' denotes scalar vector multiplication, $\hat{v}_{ni}$ is the particle velocity normal to the surface, $\mathbf{n}$ is the unit vector normal to the surface and $\hat{\mathbf{u}}_i$ is the FE displacement vector at node i. The coupling conditions for the whole model can now be written as

$$\mu \mathbf{I}_2 \frac{\partial \tilde{\boldsymbol{\Psi}}}{\partial \mathbf{n}} - \mathrm{i}\omega \mathbf{C}_2 \tilde{\mathbf{U}} = \mathbf{0} \qquad (36)$$

where the entries in $\mathbf{I}_2$ are either unity or zero. The entries in $\mathbf{C}_2$ describe either projections of the FE displacements onto the normal of the 'wetted' boundary or entries corresponding to BE degrees of freedom where the normal velocity is required to be zero, i.e. $\partial \tilde{\boldsymbol{\Psi}}/\partial \mathbf{n} = 0$.

3.3. BE solution

Eq. (36) can be rearranged to give

$$\frac{\partial \tilde{\boldsymbol{\Psi}}}{\partial \mathbf{n}} = \frac{\mathrm{i}\omega}{\mu} \mathbf{I}_2^{-1} \mathbf{C}_2 \tilde{\mathbf{U}} \qquad (37)$$

where the vector $\tilde{\mathbf{U}}(\kappa)$ consists of the displacements from the FE model. Substitution into Eq. (34) allows the velocity potential to be found at the surface nodes

$$\tilde{\boldsymbol{\Psi}} = \mathbf{H}^{-1} \mathbf{G} \frac{\partial \tilde{\boldsymbol{\Psi}}}{\partial \mathbf{n}} \qquad (38)$$

where the matrix inversion is actually a least squares solution if 'CHIEF' points are included. Having determined $\tilde{\boldsymbol{\Psi}}$ and $\partial \tilde{\boldsymbol{\Psi}}/\partial \mathbf{n}$ at the surface nodes, the pressure $\tilde{p}(\kappa)$ and particle velocity $\tilde{v}_n(\kappa)$ can be found from the Fourier transformed versions of Eqs. (28) and (29).

3.4. Radiated power

The sound power, P, radiated by the vibrating surface can be written as

$$P = \frac{1}{2} Re \left(\int_{-\infty}^{\infty} \int_{\Gamma} \hat{p}^*(x) \hat{v}_n(x) \, \mathrm{d}\Gamma \, \mathrm{d}x \right) \qquad (39)$$

where Γ is the perimeter of the cross-section A. Using Parseval's formula the integral over distance x can be expressed as an integral over wavenumber, κ,

$$P = \frac{1}{2} \, Re \left(\int_{-k}^{k} \int_{\Gamma} \tilde{p}^*(\kappa) \tilde{v}_n(\kappa) \, \mathrm{d}\Gamma \, \mathrm{d}\kappa \right) \tag{40}$$

where the integral has been limited to $-k \leqslant \kappa \leqslant k$ since larger values of κ produce no radiated power.

The results can also be presented in terms of the radiation efficiency, which can be written as

$$\sigma = \frac{P}{\frac{1}{2}\rho c \int_{-\infty}^{\infty} \int_{\Gamma} |v_n|^2 \, \mathrm{d}\Gamma \, \mathrm{d}x} \tag{41}$$

where the usual term $S\langle |v|^2 \rangle$, the squared velocity amplitude averaged over the radiating surface and multiplied by S, has been replaced by an integral since S is infinite.

3.5. Velocity normalisation

In comparing different track designs, differences in both the vibration level and the radiation efficiency are of importance. The rail vibration is induced by the wheel and rail surface roughness which forms a relative displacement excitation between wheel and rail [7]. Considering interaction in the vertical direction, the rail vibration velocity at the contact point, v_r, is given by [7]

$$v_r = \frac{\mathrm{i}\omega r Y_r}{Y_r + Y_w + Y_c} \tag{42}$$

where r is the roughness amplitude, Y_r is the mobility of the rail, Y_w is the mobility of the wheel and Y_c is the mobility of the contact spring. As a result, the wheel/rail interaction force depends on the roughness and on the point mobilities of wheel, rail and contact spring. A simplification is therefore used in order to keep the results general and avoid including models of specific wheels.

It has been noted that, in the frequency range between about 100 and 1000 Hz, the rail usually has a larger mobility than either the wheel or the contact spring [13]. The rail vibration at the contact point is therefore approximately equal to the roughness, $v_r \approx \mathrm{i}\omega r$, which can be considered as forming a velocity source. At frequencies above 1 kHz the contact spring has a higher mobility and the excitation resembles a constant force.

As the rail is usually the dominant source of noise between a few hundred Hz and 1.5 kHz [2,9,13], it is more appropriate to compare different tracks for a unit velocity excitation rather than a unit force. If P is the sound power for a unit mean-square force, the power for a unit mean-square velocity is given by

$$P_v = \frac{P}{|Y_r|^2} \tag{43}$$

where Y_r is the mobility of the rail at the forcing point ($x = 0$).

4. Results for an open rail section

The acoustic radiation from an 'open' rail section, i.e. one which is in contact with the air over its whole cross-section, is studied in this section. The result for vertical excitation at the centre of the rail-head is presented as well as results for a vertical excitation at the edge of the rail head. Furthermore, the effect of applying two different simplifications is investigated. These replicate the simplifications introduced in previously described models for rail radiation, [8,12]. Consequently, the error to which these simplifications give rise is determined.

4.1. Model and mobility

The rail profile used here is a standard CEN 40E1 section. Although this is a lighter, more flexible section than is commonly used in heavy rail applications, it is chosen for comparability with the embedded rail studied
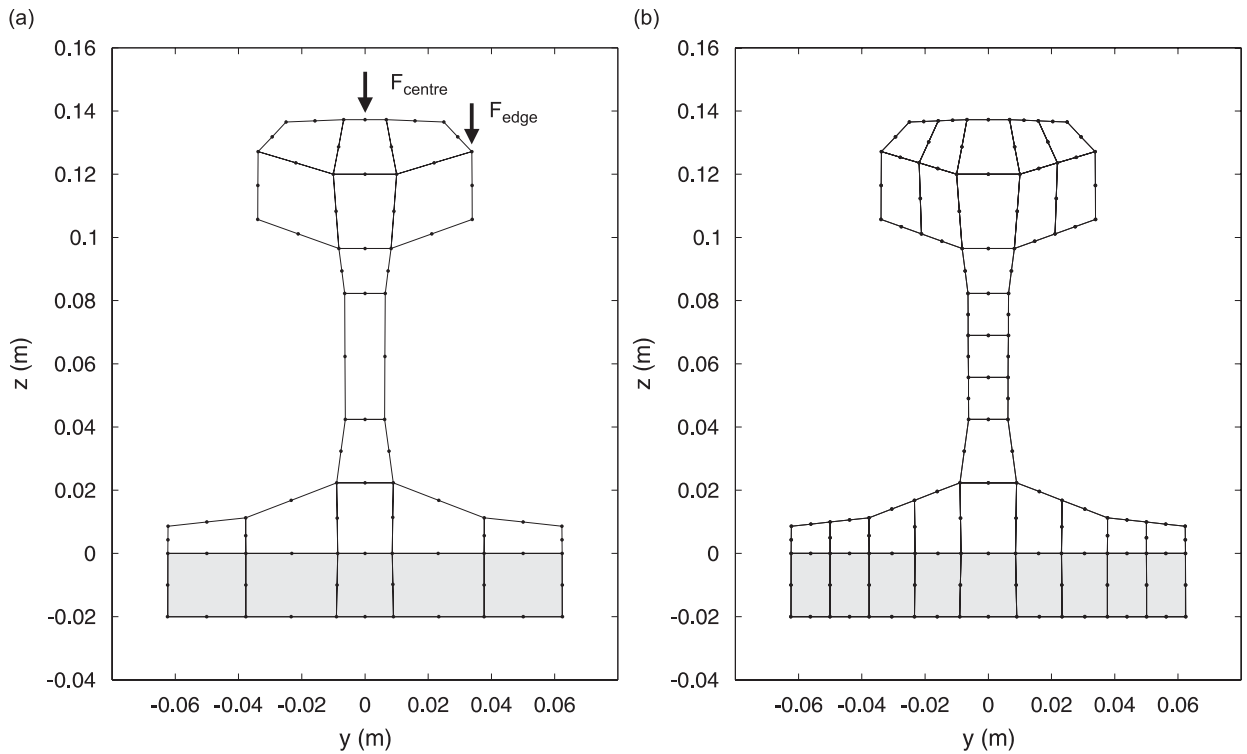
Fig. 2. Two cross-sectional models for an open rail, CEN 40E1: (a) model 1 showing central and edge excitation positions used and (b) model 2.

Table 1
Material properties used for open rail section.

	Rail	Pad
Young's modulus	210 GPa	4.8 MPa
Density (kg/m^3)	7800	10
Poisson's ratio	0.3	0.45
Damping loss factor	0.01	0.25

in Section 5. As a result the wavenumbers for the bending waves are larger than for most other rail applications and the effect of using a 2D radiation model rather than a 2D one becomes more significant.

The dimensions of the rail section can be seen from the FE mesh shown in Fig. 2 together with the two different force positions. Two different meshes are shown. The one on the left has 19 eight-noded elements and 225 degrees of freedom; the one on the right has 33 elements and 375 degrees of freedom. It was found that these two meshes give almost identical results, with differences in the radiated sound power of less than 0.3 dB up to 3.5 kHz. Therefore, the smaller mesh, Fig. 2(a), has been used in the remainder of this section.

It should be noted that the pad thickness is exaggerated in Fig. 2 compared with a real pad. This is done to clarify figures showing displacements of the rail. However, to avoid non-physical standing waves within the pad a very low density is used. The rail and pad material properties used here are given in Table 1. The pad material corresponds to a vertical support stiffness of 114 MN/m^2. Generally the rail support stiffness may vary over a large range, up to 20 times this value [37]. Although relatively low, this value is still representative of soft rail supports. It is used here, again, for the comparability with the embedded rail section. The BEs run around the circumference of the rail including the bottom of the rail foot, thus representing rail radiation as if the rail were freely suspended in air.
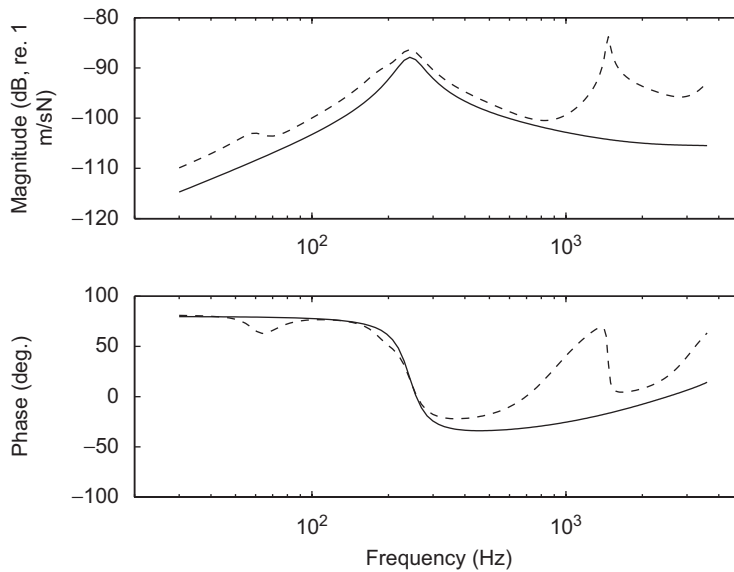
Fig. 3. Point mobilities of the open rail, CEN 40E1: —: central excitation and ---: edge excitation.
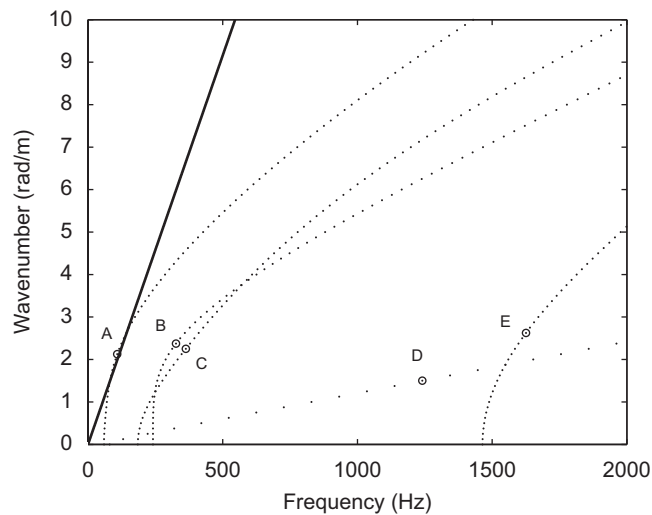

Fig. 4. Dispersion relations for the open rail, CEN 40E1. The solid line represents acoustic waves in air. Wave types marked: (a) lateral bending wave; (b) vertical bending wave; (c) torsional wave; (d) longitudinal wave; and (e) web-bending wave.

The rail vibration is calculated on the basis that the rail is continuously supported, i.e. the effects of the periodic support are neglected. This assumption is appropriate when the support stiffness is low. Even for stiffer rail pads, where the effect of periodic supports on the track response is greater, the effect on the radiated noise has been shown to be small [2].

Fig. 3 shows the 'point' mobility of the rail for the two force positions indicated in Fig. 2. This mobility is defined as the velocity at $x = 0$ divided by the total force, i.e. the force resultant from Eq. (21). The main peak, around 240 Hz, is due to the resonance of the rail mass on the stiffness of the rail pad. Below this frequency the mobility is stiffness-controlled while well above this frequency the mobility is controlled by the bending stiffness of the rail. For the forcing point away from the centre of the rail, various lateral waves are also excited (described in the next section) and the response is higher.
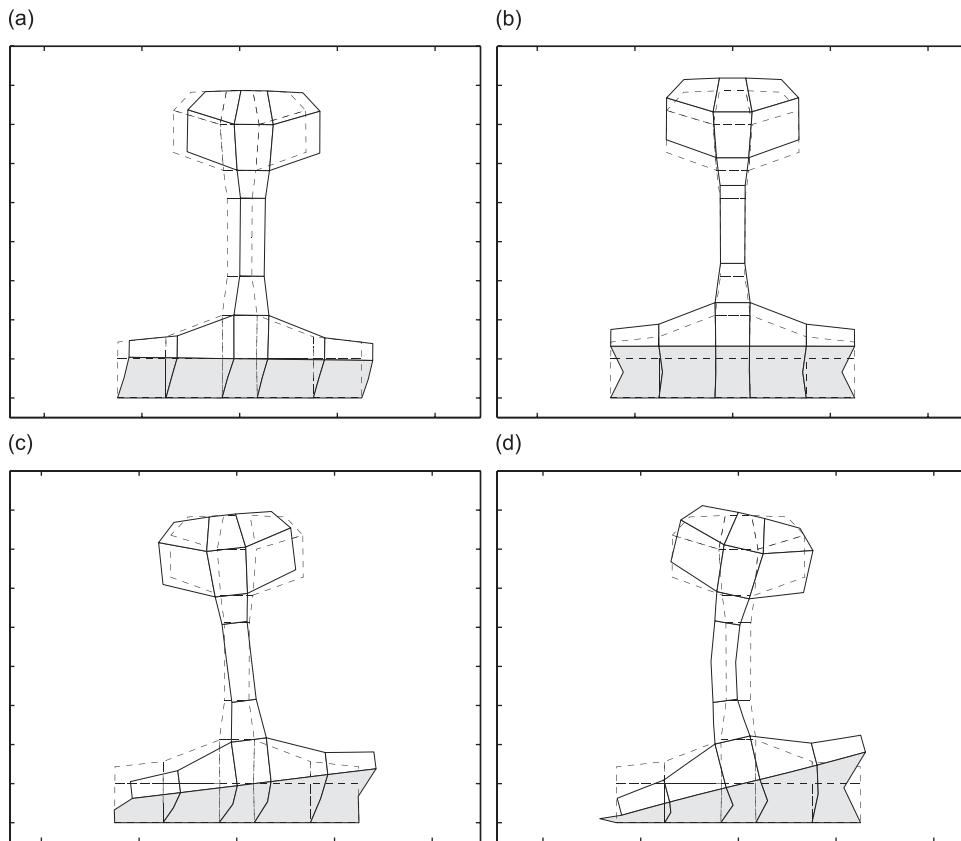
Fig. 5. Wave shapes of open rail corresponding to points indicated in Fig. 4: (a) lateral bending wave at A; (b) vertical bending wave at B; (c) torsional wave at C; and (d) web-bending wave at E.

4.2. Wave solutions

Before calculating the radiated power it is useful to consider the waves that can propagate in the rail. The dispersion relations in Fig. 4, show real valued wavenumbers, i.e. non-decaying, propagating waves, calculated for an undamped system. The dispersion relations are calculated from the eigenvalue problem stated in Eq. (18), for a range of real-valued wavenumbers κ to give the corresponding frequencies. The straight solid line is the dispersion relation for waves in air.

The deformations of the rail are given by the eigenvectors $\tilde{\mathbf{U}}_R$. These deformations in different waves are shown in Fig. 5 calculated at the wavenumber-frequency locations labelled in Fig. 4. Position 'D' in Fig. 4 corresponds to the longitudinal wave and is not shown. The vertical wave cuts on at just over 200 Hz, which is lower than usually found, due to the soft rail pads. However, its phase velocity still remains higher than that in air. Even the lateral wave, which cuts on at about 60 Hz, has a phase velocity that is mostly greater than that in air.

4.3. Radiated power

The calculated normalised power, P_v as defined in Eq. (43), for a vertical force centred at the middle of the rail is shown as the solid line in Fig. 6. The length of the excitation, β, is chosen as 9.4 mm, typical of a wheel/rail contact patch length. Below about 500 Hz, the wavelength along the rail as well as the wavelength in air is much larger than any dimension of the rail cross-section. The radiation efficiency should thus resemble that of a line dipole, i.e. showing an increase with frequency of about 30 dB per decade. The result for the case
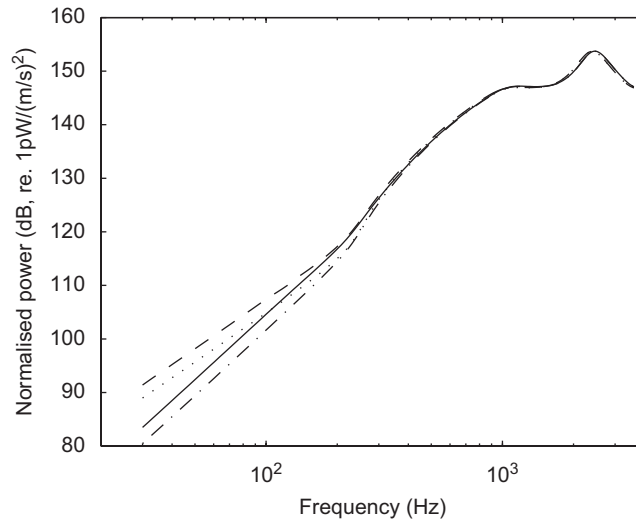
Fig. 6. Normalised powers of the open rail, CEN 40E1, for different models: —: 3D radiation; – – –: 2D radiation; – · – ·: 3D radiation with no wave cross terms; and … …: 2D radiation with no wave cross terms.
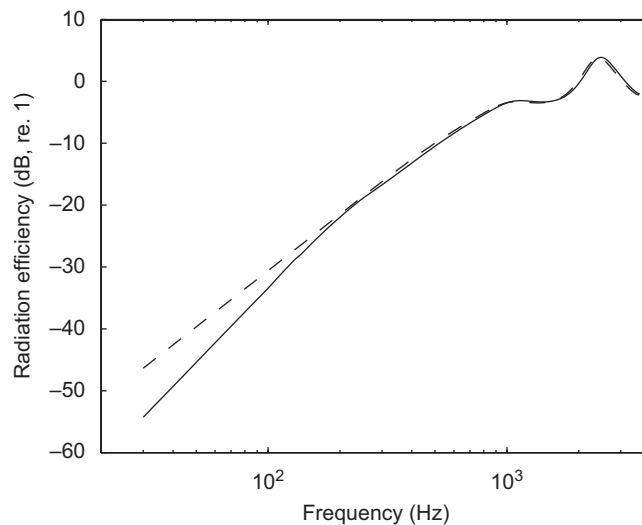

Fig. 7. Radiation efficiency for the open rail, CEN 40E1: —: 3D radiation and – – –: 2D radiation.

with a centred force is shown in Fig. 7 in the form of the radiation efficiency. As can be seen, it increases with about 30 dB per decade between 200 Hz and 1 kHz. Below the first wave cut-on, at about 200 Hz, the radiation efficiency is lower and increasing with about 40 dB per decade, as found in Ref. [12]. At frequencies above 1 kHz acoustic interference effects between the foot and the head of the rail control the radiation efficiency and various peaks and dips occur.

Two physical simplifications of the calculations, separately and combined, have also been analysed. These are: (i) 2D radiation and (ii) considering each wave to give independent contributions to the power. This leads to three additional results that are also plotted in Fig. 6. These simplifications are necessary for some other rail radiation models, e.g. those used in TWINS, [8], as presented in Appendix B. To validate this approach, the current method has been modified to encompass these physical simplifications.

The first simplification is to calculate the radiation according to a 2D BE model, i.e. with a wavenumber, $\kappa = 0$. This effect has previously been investigated in Ref. [12] where it was found that the 2D model
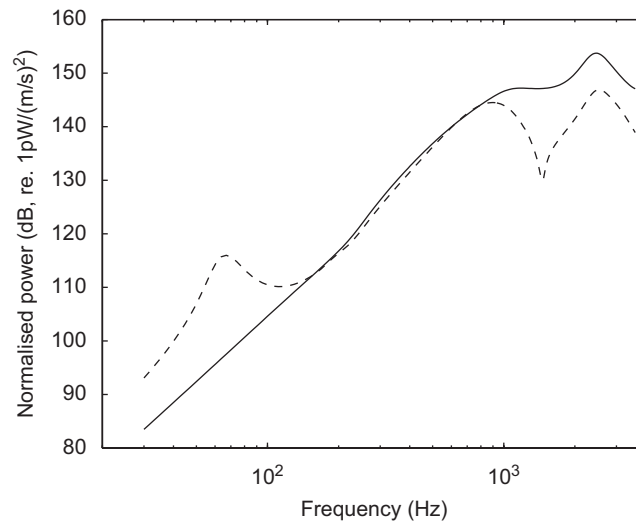
Fig. 8. Normalised powers of the open rail, CEN 40E1, for two different excitations: —: central excitation and – – –: edge excitation.

overestimates the radiation at low frequencies. On the other hand this 2D model might be expected to give larger errors when the bending wave in the rail has a wavenumber similar to that for plane waves in air. The rail section, CEN 40E1, has a low bending stiffness and therefore is more susceptible to this effect than stiffer sections. Nevertheless, the results show that the effect of this simplification is negligible above 200 Hz, the only effect being due to the change in slope of the radiation efficiency curve at low frequencies, as can be seen in Fig. 7.

The second simplification is to calculate the radiated power for each wave in the rail and then sum these contributions. Physically this is equivalent to neglecting any change in the radiation due to the inter-action (cross terms) between different waves in the rail. It has been found that this simplification has some effect at low frequencies and that the radiated power decreases when this simplification is introduced. At these low frequencies the only two waves that are of any importance are the flexural wave and the corresponding nearfield solution. Due to the pad stiffness, the flexural wave does not cut on until about 200 Hz and it is only at frequencies below this that the interaction between the waves is of any importance. Also, as can be shown analytically, after the cut-on of the vertical wave, the cross terms in the radiation disappear completely for undamped waves. Below the cut-on frequency the effect of this simplification is less than 2 dB.

As seen in Fig. 6, in the present case the two simplifications have small effects on the radiation. Moreover, they work in opposite directions and therefore tend to cancel each other to some extent. It is important to note that, in practice, at these low frequencies, the total rolling noise from the track is often dominated by noise from sleepers [2].

Another feature of interest that has not been fully explored in previous research is the effect of the rotational and web-bending waves seen in Fig. 5. Again a worst case scenario is sought. For this reason the force is moved to the edge of the rail-head as shown in Fig. 2(a). The power for a unit velocity at the excitation point is compared for this case and the centred excitation case in Fig. 8.

As can be seen, the edge excitation apparently decreases the radiated power in much of the frequency range. At low frequencies (below 200 Hz), where the lateral wave dominates, there is an increase in radiated power, whereas at high frequencies, where the web-bending wave has cut on there is a large reduction. However, the latter effect is primarily due to the normalisation with the rail velocity. The velocity level at the excitation point increases when the forcing point is moved to the edge of the rail, as seen in Fig. 3. Therefore the normalised power, P_v, decreases correspondingly. Since the additionally excited rotational and web-bending waves radiate little acoustic power, models not including this radiation should still be usable as long as the mobility of the rail is correctly predicted.

5. Results for an embedded rail section

The sound power radiated from an embedded tram rail is studied in this section. The embedded rail is deliberately chosen to have similar dynamic properties to the open rail. This enables comparisons of radiated power between the two track types.

5.1. Model and mobility

The rail is a standard CEN 51Ri profile used for trams and the embedding is made to fill the space around this profile as shown in Fig. 9. As can be seen two different embedding materials are used; a softer 'pad' and a stiffer 'fill' material around the rail. Similar configurations have been used for recently built tramways.

The vertical stiffness is virtually the same as that for the previously discussed open rail. The properties of the embedding materials are shown in Table 2. The rail is made of steel and its material properties are the same as those previously given in Table 1. The excitation length, β, is 9.4 mm, as before.

The mesh is such that the maximum distance between adjacent nodes is about 16 mm. In fact slightly larger distances between nodes occur on the rail surface but here the rail will constrain the rubber. The shear wave speed in the 'fill' material is 70.3 m/s. Results from this model will therefore only be shown below 1100 Hz. In this frequency range, there are at least four nodes per wavelength; in the vertical direction, which is the most important, there are at least six. In the 'pad' material the shear wave speed is lower at 37 m/s. Here the
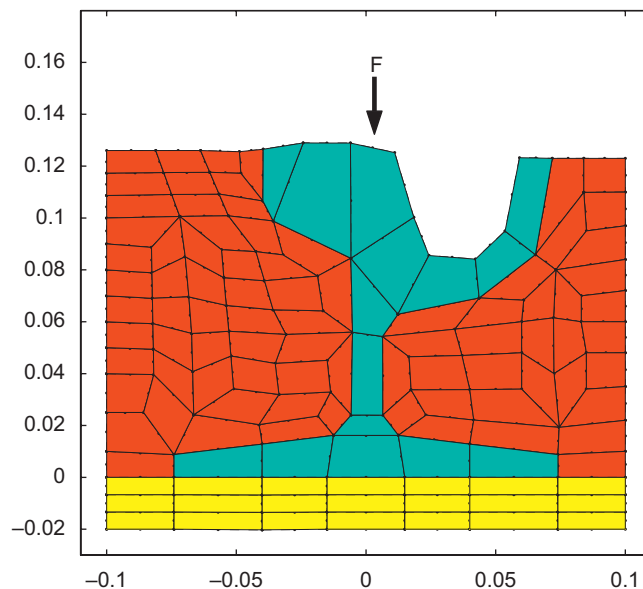

Fig. 9. Model mesh of embedded rail section.

Table 2
Material properties used for embedding materials: 'pad' refers to the material below the rail foot and 'fill' to the material beside the rail.

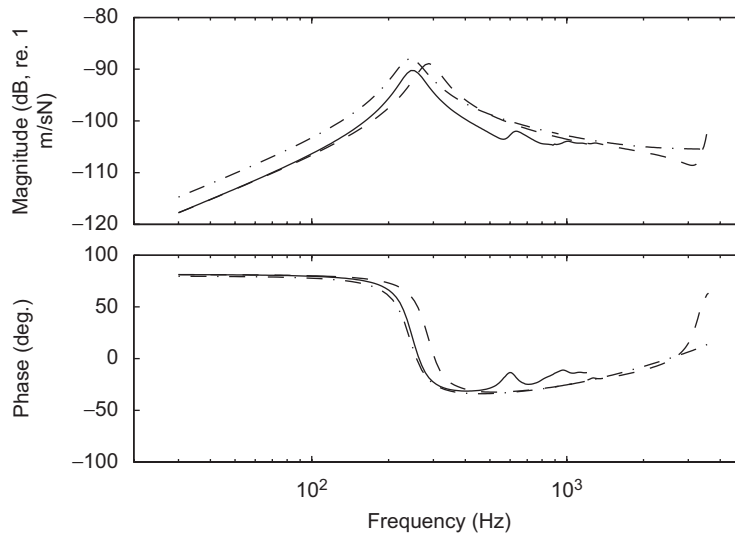|	Pad	Fill
Young's modulus (MPa)	4.0	20
Density (for normal mass embedding) (kg/m^3)	1000	1500
Density (for reduced mass embedding) (kg/m^3)	1.0	1.5
Poisson's ratio	0.45	0.35
Damping loss factor	0.25	0.15

Fig. 10. Point mobilities of the two rail sections: —: CEN 51Ri with normal mass embedding; – – –: CEN 51Ri with reduced mass embedding; and – · – · : open rail CEN 40E1.

elements are strictly too large in the width direction, but since the motion of interest is vertical in this region, the element density is sufficient up to about 2 kHz.

The point mobility of the rail is shown in Fig. 10. The point mobility for the same rail system but with the mass of the embedding material reduced to 0.1% of the original is also shown. This analysis was included so that waves existing primarily in the embedding material would not cut on in the frequency range considered. Since the two curves are similar, it is concluded that waves propagating primarily in the embedding material have only limited effect on the mobility of the rail. The mobility for the open rail section with the force at the centre of the railhead is also shown for comparison. The difference between this curve and the other two is relatively small. This indicates that the dynamics for the open and the embedded rails are roughly equivalent. Hence, the noise radiation levels from the open and embedded rail systems can be compared directly in that, from a dynamic perspective, the tracks are almost interchangeable.

The embedded rail with the reduced-mass embedding material shows similar behaviour to the open rail, although its resonance frequency is slightly higher and the stiffness-controlled mobility at low frequencies is slightly lower. The mobility rises towards a peak at about 3.4 kHz, which corresponds to a higher order rail mode with large deformation of the rail foot.

The embedded rail model with normal mass embedding material shows the same stiffness-controlled behaviour at low frequencies. The resonance frequency is similar to that of the open rail but lower than that for the reduced-mass embedding due to the additional mass. With the normal mass embedding the mobility above 300 Hz is lower than the other two results. Above 600 Hz the extra mass decouples through a series of waves in the embedding material and the mobility converges towards the other results.

5.2. Wave solutions

Dispersion relations and wave shapes can be calculated in the same manner as in the previous section. The dispersion relations for the embedded rail are shown in Fig. 11. Again the solid line represents the dispersion relation for air, i.e. $k = \omega/c$.

As can be seen from this figure, there are many waves that cut on at frequencies above about 500 Hz. Most of these waves are predominantly in the embedding material. In order to examine the effect these waves have, the behaviour is compared with that of the model with very low mass in the embedding materials, as discussed in Section 5.1. The dispersion relations then portray the behaviour of the rail only. These are shown in Fig. 12.
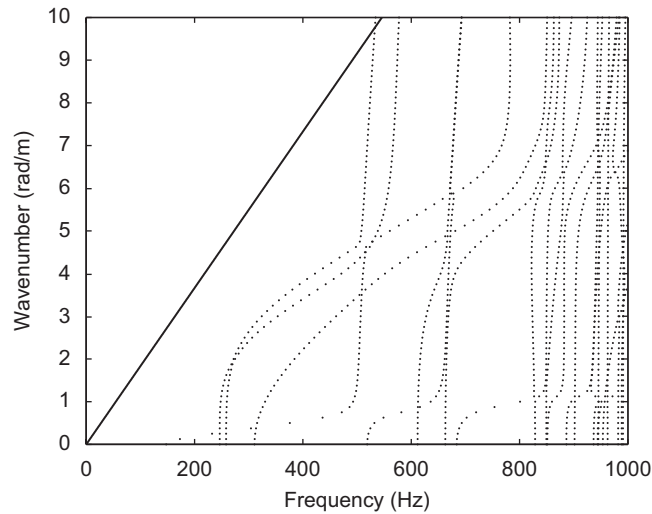
Fig. 11. Dispersion relations of the waves in the CEN 51Ri rail, embedded with the normal mass. The solid line represents acoustic waves in air.
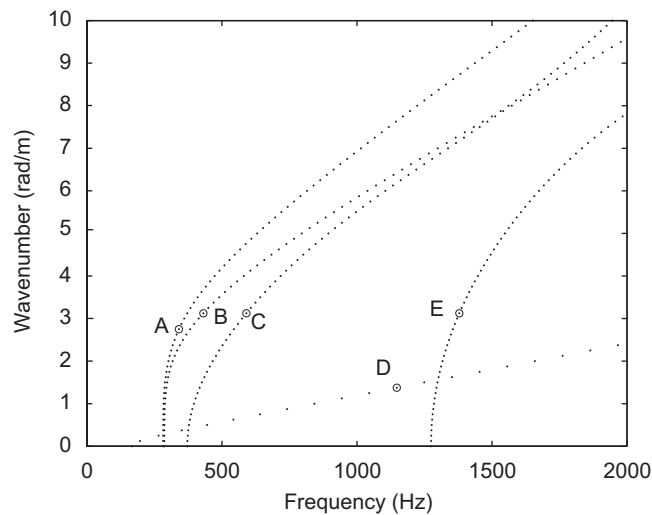

Fig. 12. Dispersion relations of the waves in the CEN 51Ri rail, embedded with the reduced mass. Wave types marked: (a) lateral bending wave; (b) vertical bending wave; (c) torsional wave; (d) longitudinal wave; and (E) web-bending wave.

The wave shapes at the points indicated in Fig. 12 are plotted in Fig. 13. As before, the actual shapes are 3D although the wave shapes are only shown in 2D plots. Similar results are found for the corresponding waves from the model including the full mass filler material and the material with reduced mass. In these waves the embedding material is driven by the vibration of the rail with no dynamic effects within its own bulk. The vertical wave cuts on at a similar frequency to the open rail, but the lateral wave cuts on at a higher frequency, similar to that of the vertical wave, due to the influence of the stiffness of the 'fill' material.

The rail decay rates (see Appendix B) are shown in Fig. 14. The upper graph shows the results for the reduced mass embedding and the lower graph that for the normal mass case. The cut-on frequencies correspond to the frequencies where the curves in Fig. 14 drop sharply. The longitudinal wave, curve D, which has the lowest cut-on frequency at about 150 Hz, also has the lowest decay rate. The three curves, A, B and C, dropping between about 200 and 300 Hz, correspond to the two flexural waves and the torsional wave in the rail. Curve E, which cuts on above 1 kHz, corresponds to the web bending wave.
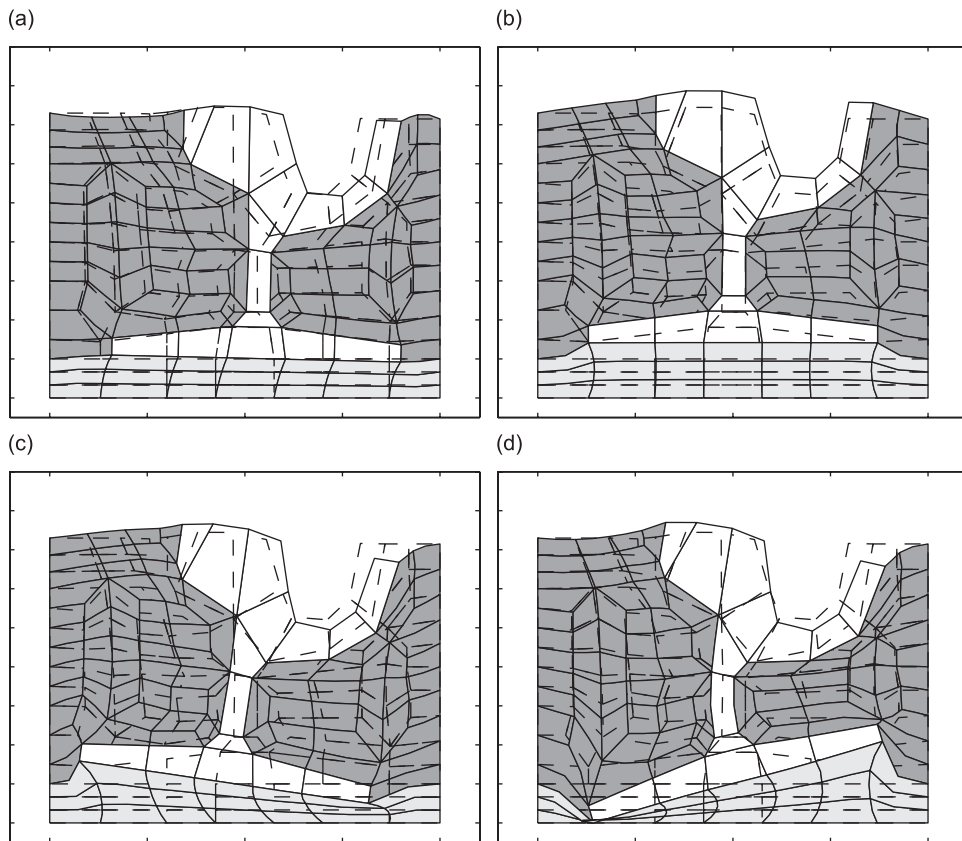
(a) (b)

(c) (d)

Fig. 13. Wave shapes of embedded rail corresponding to points indicated in Fig. 12: (a) lateral bending wave; (b) vertical bending wave; (c) torsional wave; and (e) web-bending wave. The embedding material has negligible mass.
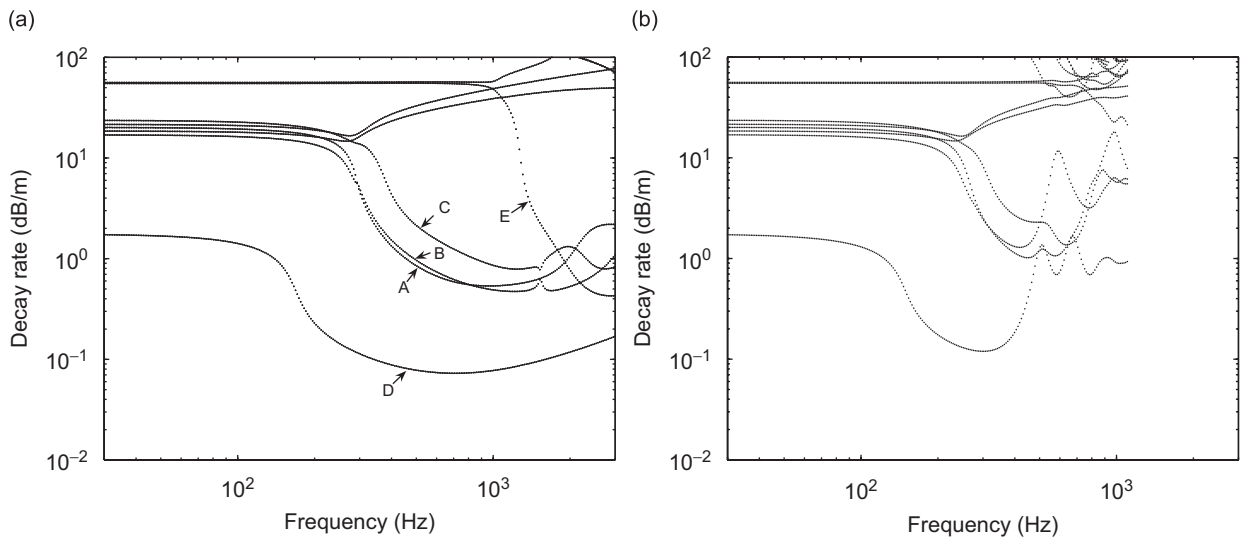
(a) (b)

Fig. 14. Decay rates of waves in the CEN 51Ri rail with: (a) the reduced mass embedding and (b) the normal mass embedding.

The mass of the embedding material can be seen in Fig. 14(b) to reduce the cut-on frequencies and to lead to increased decay rates above about 500 Hz due to interaction between the rail and waves in the embedding material.

5.3. Radiated power

The radiated power from the embedded rail, normalised by the velocity of the rail at the excitation point, is shown in Fig. 15. Compared with the results for the open rail, shown in Fig. 6, the radiated power for the normal embedding is lower at frequencies above about 600 Hz.

At frequencies below 600 Hz, however, the normalised radiated power from the embedded rail is higher than for the open rail. Since the embedded rail radiates only from its upper surface, it displays a line monopole radiation characteristic, whereas the open rail has a line dipole radiation character, as noted previously. This difference can be seen clearly in Fig. 16 where the radiation efficiency of the embedded rail can be seen to have a much lower slope than the open rail, and consequently a much higher radiation efficiency at low frequencies.

From Fig. 15 it is seen that the radiated power for the proper embedding model drops below that of the low mass embedding model for frequencies above 500 Hz. Since the point mobility is almost the same (Fig. 10),
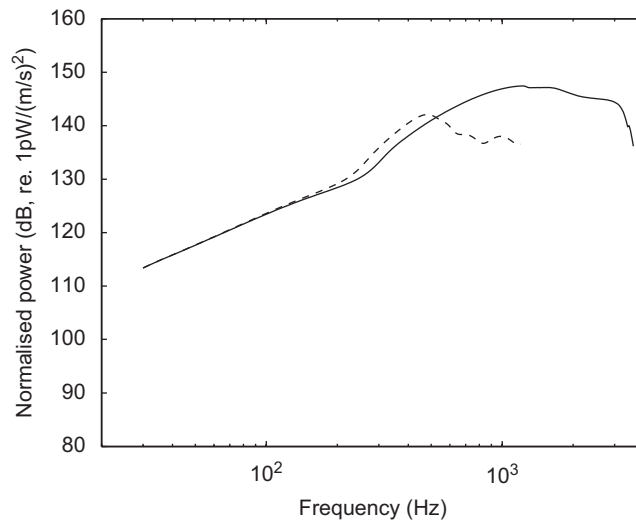

Fig. 15. Normalised power of the embedded rail with different embedding conditions: —: reduced mass embedding and – – –: normal embedding.
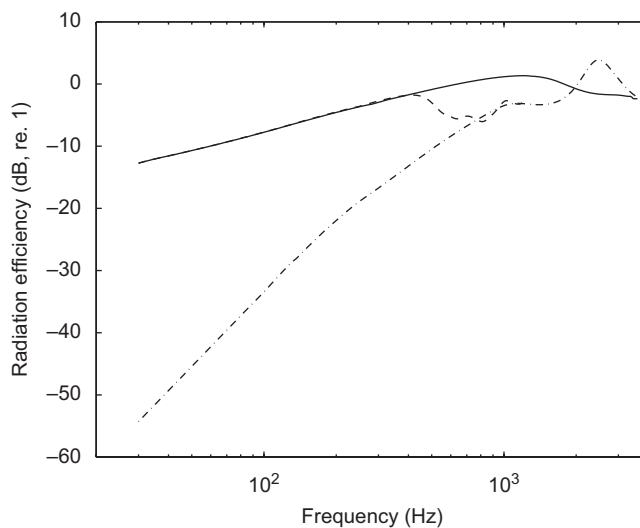

Fig. 16. Comparison of radiation efficiencies obtained from the embedded and open rails: —: CEN 51Ri with reduced mass embedding; – – –: CEN 51Ri with normal mass embedding; and – · – ·: the open rail CEN 40E1.

there are two possible explanations for this. Clearly, the coupling between the rail and the embedding material results in a higher decay rate, as already seen in Fig. 14. In addition, it is possible that the motion of the surface of the embedding material may result in a modified radiation due to acoustic short-circuiting effects. The extent to which the latter phenomena is relevant needs some further investigation.

As has been noted, with the low mass embedding material, the rail will act as a line monopole throughout most of the frequency range considered. When the mass of the embedding is included this will change. The vertical bending wave is shown at two different frequencies in Fig. 17. At 518 Hz the embedding material moves in phase with the rail and at a greater amplitude, whereas at 810 Hz it moves out of phase with the rail and hence the radiation from these parts to some extent will cancel each other. For the low mass embedding material the free surface always vibrates in phase with the rail.

The normal radiation efficiency, Eq. (41), will not give a good comparison between cases with and without the mass of the embedding material. This is because large velocity amplitudes of the embedding material will lower the radiation efficiency regardless of the radiated power. Therefore, an 'adjusted' radiation efficiency is used instead. This is defined in the same way as the normal radiation efficiency, except that the averaged squared velocity in the denominator is taken only over the exposed part of the rail surface, that is

$$\sigma_a = \frac{P}{\frac{1}{2}\rho_0 c S_r \langle |v_r|^2 \rangle} \tag{44}$$

where subindex 'a' means 'adjusted' and subindex 'r' means rail.

The 'normal' radiation efficiency, defined through Eq. (41), and the 'adjusted' radiation efficiencies for the high and low mass embedding models are compared in Fig. 18. The results for σ_a for the reduced mass
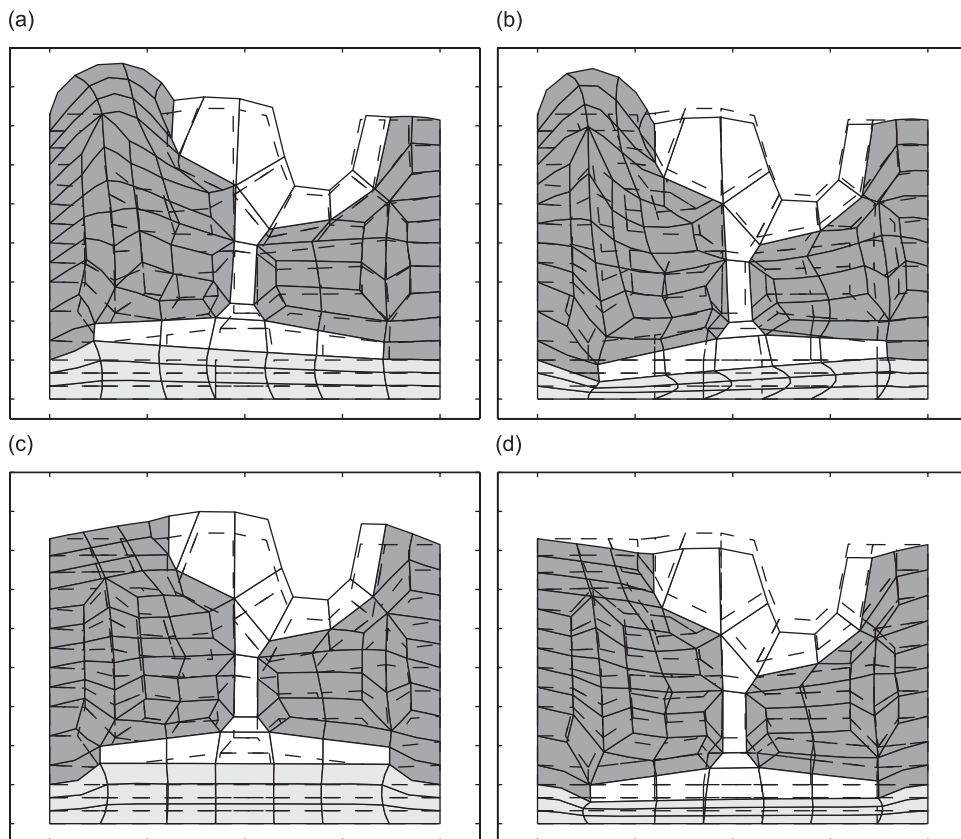

Fig. 17. Wave shapes of vertical bending wave of embedded rail: (a) normal embedding, 518 Hz; (b) normal embedding, 810 Hz; (c) reduced mass embedding, 518 Hz; and (d) reduced mass embedding, 810 Hz.
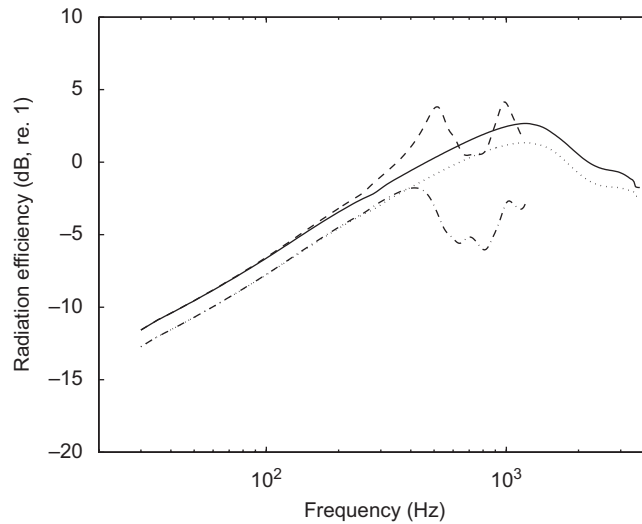
Fig. 18. Radiation efficiencies of the embedded rail with different embedding conditions: ……: reduced mass embedding; – · – ·: normal embedding; —: adjusted radiation efficiency for reduced mass embedding; and – – –: adjusted radiation efficiency for normal embedding.

embedding are similar to those for σ, apart from a constant difference in level caused by the change in surface area.

It can be seen that, for the normal mass embedding model, the adjusted radiation efficiency is considerably greater than for the reduced mass case around 500 and 1000 Hz but is lower between 700 and 900 Hz. The increases at 500 (and 1000) Hz can be associated with large amplitude motion of the embedding material in phase with the rail, Fig. 17(a), whereas the reductions correspond to situations where the embedding material moves out of phase with the rail, Fig. 17(b). Although the adjusted radiation efficiency shows increases at some frequencies, this is compensated by increases in decay rate, leading to the overall reduction in normalised power seen in Fig. 15.

Overall, therefore, comparing Fig. 8 and Fig. 15 shows that embedded rails have the prospect of being quieter than open rails in the frequency range 500–2000 Hz which is important for noise from the rail. However, this is mainly due to the increased decay rate, partly offset by increases in the (adjusted) radiation efficiency.

6. Conclusions

A novel method to calculate the noise radiated from rails is described in this paper. The method is based on waveguide finite elements and wavenumber boundary elements and, for considering the characteristics of radiation from waves in rails, it is more comprehensive than other rail radiation methods found in the literature.

Computations of acoustic radiation from open rails have been shown to be little influenced by physical simplifications introduced in previous models. Some small discrepancies associated with these simplifications have been found for low frequencies, but for practical use these discrepancies are likely to be negligible. Also, for rails excited at the edge of the railhead, it has been found that higher order waves increase the point mobility of the rail, whereas their effect on radiated power is relatively small.

The embedded track considered is found to radiate less power than an open rail above about 600 Hz when the mass of the embedding material is included in the calculations. This is mainly due to an increased decay rate of the waves in the rail, resulting in lower vibration levels. At some frequencies the free surface of the embedding material amplifies the sound radiation while at others some cancellation occurs when it vibrates out of phase with the rail. These two effects indicate the possibility that embedded rail systems may emit considerably lower noise levels than more conventional open rails if appropriately designed.

At low frequencies, however, an embedded rail may radiate more noise than an open rail, since the radiation characteristic of the embedded rail displays a line monopole radiation behaviour compared with the line dipole behaviour of a conventional open rail.

Acknowledgement

Appendix A

The stiffness tensor $\mathbf{D}$ in Eq. (2) is given by

$$\mathbf{D} = \frac{E}{(1+v)(1-2v)} \begin{bmatrix} 1 & v & v & 0 & 0 & 0 \\ v & 1 & v & 0 & 0 & 0 \\ v & v & 1 & 0 & 0 & 0 \\ 0 & 0 & 0 & \frac{1}{2}-v & 0 & 0 \\ 0 & 0 & 0 & 0 & \frac{1}{2}-v & 0 \\ 0 & 0 & 0 & 0 & 0 & \frac{1}{2}-v \end{bmatrix} \tag{A.1}$$

The tensor operators $\mathbf{B}_0$ and $\mathbf{B}_1$ in Eq. (3) are given by

$$\mathbf{B}_0 = \begin{bmatrix} 0 & 0 & 0 \\ 0 & \frac{\partial}{\partial y} & 0 \\ 0 & 0 & \frac{\partial}{\partial z} \\ \frac{\partial}{\partial y} & 0 & 0 \\ \frac{\partial}{\partial z} & 0 & 0 \\ 0 & \frac{\partial}{\partial z} & \frac{\partial}{\partial y} \end{bmatrix} \quad \text{and} \quad \mathbf{B}_1 = \begin{bmatrix} 1 & 0 & 0 \\ 0 & 0 & 0 \\ 0 & 0 & 0 \\ 0 & 1 & 0 \\ 0 & 0 & 1 \\ 0 & 0 & 0 \end{bmatrix} \tag{A.2}$$

Appendix B

The method used to estimate the sound radiation by the rail in the TWINS model [8,9] is summarised here. The rail vibration is described by a series of damped, propagating waves. The radiation is calculated separately for each wave, using

$$P_{\text{wave}} = \frac{1}{2} \rho c \sigma_{2D} \int_{-\infty}^{\infty} \int_{\Gamma} |v_{\text{wave}}|^2 \, \mathrm{d}\Gamma \, \mathrm{d}x \tag{B.1}$$

where $v_{\text{wave}}(x)$ is the velocity amplitude in the wave, σ_{2D} is the 2D radiation efficiency. For a wave with a complex wavenumber $\kappa = k_{\text{wave}} - \mathrm{i}\beta_{\text{wave}}$, the vibration is

$$v_{\text{wave}}(x) = v_{\text{wave}}(0)\mathrm{e}^{-\mathrm{i}k_{\text{wave}}|x|}\mathrm{e}^{-\beta_{\text{wave}}|x|} \tag{B.2}$$

and the integral over x can be determined as

$$\int_{-\infty}^{\infty} |v_{\text{wave}}|^2 \, \mathrm{d}x = |v_{\text{wave}}(0)|^2 \int_{-\infty}^{\infty} \mathrm{e}^{-2\beta_{\text{wave}}|x|} \, \mathrm{d}x = \frac{|v_{\text{wave}}(0)|^2}{\beta_{\text{wave}}} \tag{B.3}$$

The sound power from each wave can then be added.

As seen in Eq. (B.3) the imaginary parts of the wavenumbers, $Im\{\kappa\} = \beta_{\text{wave}}$ are very important for the rail noise radiation. These are directly related to the 'decay rates', d, given in dB/m as

$$d = 20 \log_{10}(e)\beta_{\text{wave}} = 8.686\beta_{\text{wave}} \tag{B.4}$$

The sound power is thus inversely proportional to the decay rates. Within the TWINS model the rail sound radiation is determined by calculating the wave amplitudes $v_{\text{wave}}(0)$ due to the interaction force, the wave decay rates, d, and the 2D radiation efficiency, σ_{2D}, and combining them according to the above formulae. This introduces some approximations which are assessed in the present paper.

References

[1] D.J. Thompson, Predictions of acoustic radiation from vibrating wheels and rails, *Journal of Sound and Vibration* 120 (1988) 275–280.

[2] D.J. Thompson, C.J.C. Jones, Review of the modelling of wheel/rail noise generation, *Journal of Sound and Vibration* 231 (2000) 519–536.

[3] B.P. Temple, E del Rio Alonso, Design and development of the Balfour Beatty embedded slab track system, *Railway Engineering, Seventh International Conference*, London, 2004.

[4] H. Holzinger, M. Kieninger, D. Prochaska, H. Steinfeld, S. Bruni, P. Folgarait, M. Teas, Design of a high performance slab track, *Railway Engineering, Seventh International Conference*, London, 2004.

[5] P.J. Remington, Wheel/rail noise, part IV: rolling noise, *Journal of Sound and Vibration* 46 (1976) 419–436.

[6] P.J. Remington, Wheel/rail rolling noise, I: theoretical analysis, *Journal of the Acoustical Society of America* 81 (1987) 1805–1823.

[7] D.J. Thompson, Wheel-rail noise generation, part I: introduction and interaction model, *Journal of Sound and Vibration* 161 (1993) 387–400.

[8] D.J. Thompson, B. Hemsworth, N. Vincent, Experimental validation of the TWINS prediction program for rolling noise, part 1: description of the model and method, *Journal of Sound and Vibration* 193 (1996) 123–135.

[9] D.J. Thompson, P. Fodiman, H. Mahé, Experimental validation of the TWINS prediction program for rolling noise, part 2: results, *Journal of Sound and Vibration* 193 (1996) 137–147.

[10] D.J. Thompson, Wheel-rail noise generation, part III: rail vibration, *Journal of Sound and Vibration* 161 (1993) 421–446.

[11] D.J. Thompson, N. Vincent, Track dynamic behaviour at high frequencies. Part 1: theoretical models and laboratory measurements, *Vehicle System Dynamics* (Suppl. 24) (1995) 86–99.

[12] D.J. Thompson, C.J.C. Jones, N. Turner, Investigation into the validity of two-dimensional models for sound radiation from waves in rails, *Journal of the Acoustical Society of America* 113 (2003) 1965–1974.

[13] D.J. Thompson, P.E. Gautier, A review of research into wheel/rail rolling noise reduction, *Proceedings of the Institution of Mechanical Engineers—Part F: Journal of Rail and Rapid Transit* 220F (2006) 385–408.

[14] B. Aalami, Waves in prismatic guides of arbitrary cross section, *Journal of Applied Mechanics* 40 (1973) 1067–1072.

[15] S.K. Datta, A.H. Shah, R.L. Bratton, T. Chakraborty, Wave propagation in laminated composite plates, *Journal of the Acoustical Society of America* 83 (1983) 2020–2026.

[16] L. Gavric, Finite element computation of dispersion properties of thin-walled waveguides, *Journal of Sound and Vibration* 173 (1994) 113–124.

[17] U. Orrenius, S. Finnveden, Calculation of wave propagation in rib-stiffened plate structures, *Journal of Sound and Vibration* 198 (1996) 203–224.

[18] S. Finnveden, Spectral finite element analysis of the vibration of straight fluid-filled pipes with flanges, *Journal of Sound and Vibration* 199 (1) (1997).

[19] C.-M. Nilsson, Waveguide Finite Elements Applied on a Car Tyre, Doctoral Thesis, MWL, KTH, Stockholm, 2004.

[20] K. Knothe, Z. Strzyzakowski, K. Willner, Rail vibrations in the high frequency range, *Journal of Sound and Vibration* 169 (1994) 111–123.

[21] L. Gavric, Computation of propagative waves in free rail using a finite element technique, *Journal of Sound and Vibration* 185 (1995) 531–543.

[22] I. Bartoli, A. Marzani, F. Lanza di Scalea, E. Viola, Modeling wave propagation in damped waveguides of arbitrary cross-section, *Journal of Sound and Vibration* 295 (2006) 685–707.

[23] J. Ryue, D.J. Thompson, P.R. White, D.R. Thompson, Investigations of propagating wave types in railway tracks at high frequencies, *Journal of Sound and Vibration* 315 (2008) 157–175.

[24] L. Gry, Dynamic modelling of railway track based on wave propagation, *Journal of Sound and Vibration* 195 (1996) 477–505.

[25] L. Gry, C. Gontier, Dynamic modelling of railway track: a periodic model based on a generalized beam formulation, *Journal of Sound and Vibration* 199 (1997) 531–558.

[26] J. Gomez, E.G. Vadillo, J. Santamaria, A comprehensive track model for the improvement of corrugation models, *Journal of Sound and Vibration* 293 (2006) 522–534.

[27] D. Duhamel, Efficient calculation of the three-dimensional sound pressure field around a noise barrier, *Journal of Sound and Vibration* 197 (5) (1996) 547–571.

[28] S.N. Chandler-Wilde, The boundary element method in outdoor noise propagation (Tyndall Medal Lecture), *Proceedings of the Institute of Acoustics* 19 (1997) 27–50.

[29] D.S. Malkus, R.D. Cook, M.E. Plesha, *Concepts and Applications of Finite Element Analysis*, third ed., Wiley, Cop, 1988.

[30] G. Strang, *Introduction to Applied Mathematics*, Wellesley-Cambridge Press, Cop, 1986.

[31] F. Tisseur, K. Meerbergen, The quadratic eigenvalue problem, *SIAM Review* 43 (2001) 235–286.

[32] I. Karassalo, Exact finite elements for wave propagation in range-independent fluid–solid media, *Journal of Sound and Vibration* 172 (1994) 671–688.

[33] S. Finnveden, C.-M. Nilsson, Input power to waveguides calculated by a finite element method, *Journal of Sound and Vibration* 305 (2007) 641–658.

[34] S. Temkin, *Elements of Acoustics*, Wiley, New York, 1981.

[35] T.W. Wu, *Boundary Element Acoustics*, WIT Press, 2000.

[36] H.A. Schenck, Improved integral formulation for acoustic radiation problem, *Journal of the Acoustical Society of America* 44 (1968) 41–58.

[37] D.J. Thompson, J.W. Verheij, The dynamic behaviour of rail fasteners at high frequencies, *Applied Acoustics* 52 (1997) 1–17.